CHEMIJA
2026. Vol. 37. No. 3. P. 225–243

ISSN 0235-7216 eISSN 2424-4538
DOI: https://doi.org/10.6001/chemija.2026.37.3.5

Stereolithography-derived boron nitride-based 3D photocatalysts with controlled architectures for water treatment

Petras Rauka,

Robertas Virkėtis,

Simas Šakirzanovas,

Greta Merkininkaitė*

Institute of Chemistry,
Faculty of Chemistry and Geosciences,
Vilnius University, 24 Naugarduko Street,
03225 Vilnius, Lithuania

A novel boron nitride (BN) containing composite photoresin was developed and used to fabricate BN-based three-dimensional (3D) photocatalysts with controlled geometries via stereolithography (SLA), followed by pyrolysis. Three architectures – gyroid, honeycomb and cubic lattice structures with different structural periodicities – were produced and characterised. The influence of 3D architecture on structural integrity and photocatalytic performance was evaluated through the degradation of Rhodamine B (RhB) under halogen lamp irradiation. The photocatalytic performance strongly depended on the architecture, with increasing structural periodicity leading to a higher density of fabrication defects, a reduced solution permeability, and a lower accessible active surface area. Among all investigated structures, the 2 × 2 cubic lattice exhibited the highest photocatalytic performance, achieving 88.44% RhB degradation after 150 min of halogen lamp irradiation and the highest surface area-normalised efficiency of 259.9 mg/m^2. These findings demonstrate that additive manufacturing enables the fabrication of efficient, reusable, self-supporting h-BN-based photocatalysts.

Keywords: boron nitride, stereolithography, pyrolysis, 3D photocatalysts, photocatalysis

INTRODUCTION

The rapid growth of the global population has intensified the challenge of providing access to safe drinking water, particularly in low-income and developing regions. In many of these areas, communities rely on surface water sources that are frequently contaminated with pathogenic bacteria, protozoa, and other harmful microorganisms, posing significant risks to human health. Conventional water treatment technologies are often insufficiently effective, economically inaccessible, or associated with secondary environmental pollution [1–3]. Consequently, there is a growing demand for sustainable, cost-effective, and environmentally friendly approaches to water purification.

Among water treatment technologies, photocatalytic purification has attracted a considerable attention due to its ability to degrade organic pollutants and inactivate microorganisms using solar energy. However, the practical application of widely used photocatalytic materials is often limited by a low photocatalytic activity, a rapid charge-carrier recombination, and an insufficient long-term stability [4]. As a result, significant research efforts have been directed toward the development of highly efficient photocatalysts, including those based on hexagonal boron nitride (h-BN). Owing to its unique physicochemical properties, h-BN has emerged as a promising material for photocatalytic applications [5].

* Corresponding author. Email: greta.merkininkaite@chgf.vu.lt

To date, particulate and membrane-based photocatalysts have been the most commonly investigated systems for photocatalytic water treatment. However, these approaches typically require additional post-treatment filtration steps to remove catalyst particles from the purified water, increasing process complexity and operational costs [6]. Therefore, the development of reusable and durable photocatalytic structures remains an important objective [7, 8].

Recent advances in additive manufacturing technologies offer new opportunities for the fabrication of photocatalytic materials with tailored geometries and enhanced functionality. In particular, stereolithography (SLA) enables the production of complex three-dimensional (3D) structures with high precision and controllable architectures, making it a promising technique for manufacturing reusable photocatalysts [9]. Importantly, structural parameters such as porosity, surface area, and overall geometry can significantly influence photocatalytic performance by affecting light propagation, the availability of active sites, and mass transport processes [10–12]. Therefore, investigating the feasibility of fabricating h-BN-based 3D photocatalytic structures via SLA and evaluating their photocatalytic efficiency are essential for advancing their application in water purification technologies.

In this work, we fabricated boron nitride-based photocatalysts with controlled three-dimensional architectures and investigated their structural, physicochemical and photocatalytic properties. It was found that photocatalysts produced using this approach are comparable in performance to conventionally used systems. The most efficient was the 2 × 2 cubic lattice h-BN photocatalyst, which achieved 88.44% degradation of RhB after 150 min of irradiation under a halogen lamp.

EXPERIMENTAL

Reagents

The following materials were used in this study: boron nitride (BN, 98%, Sigma-Aldrich), 2-hydroxyethyl methacrylate (HEMA, $C_6H_{10}O_3$, Sigma-Aldrich, 97%), trimethylolpropane ethoxylate triacrylate (TMPEOTA, $C_{21}H_{32}O_9$, Sigma-Aldrich, ≤100%), and trimethylbenzoyl diphenylphosphine oxide (TPO, $C_{22}H_{21}O_2P$, 99%, BLD Pharmatech Ltd.).

Material preparation

A photopolymer resin was prepared in a 250 mL glass beaker by mixing 45.79 mL of HEMA (0.3765 mol, density 1.07 g/cm^3) and 44.54 mL of TMPEOTA (0.1140 mol, density 1.10 g/cm^3), together with 2 wt.% of the photoinitiator TPO. The resin was homogenised by stirring at room temperature on a magnetic stirrer for 10 min at 400 rpm. After stopping the stirring, 25.0 g of BN (1.01 mol) was gradually added to the resin, and the mixture was further stirred for 15 min at 400 rpm to ensure uniform dispersion of the filler. The resulting resin was subsequently used for SLA 3D printing.

Stereolithography 3D printing and thermal processing

A series of 3D structures, including honeycomb, cubic lattice, and gyroid geometries (see Fig. 1), were fabricated using a Prusa SL1S SPEED 3D printer (LED wavelength 405 nm). The designed dimensions of all structures were 20 × 20 × 20 mm. The printing parameters were as follows: layer thickness of 0.025 mm, exposure time of 300 s for the first eight layers, and 30 s for all subsequent layers. The layer instructions for printing were generated

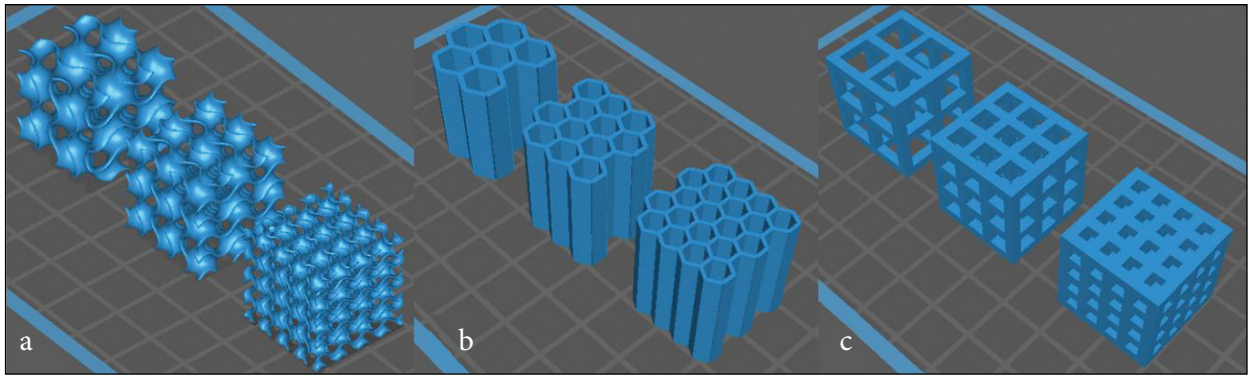

Fig. 1. Models of the 3D structures used in this study: (a) gyroid structures, (b) honeycomb lattice structures and (c) cubic lattice structures

using the PrusaSlicer software. After printing, uncured resin was removed by washing the structures in isopropanol for 20 min, followed by post-curing for 30 min. Both the washing and post-curing processes were performed using an Anycubic Wash & Cure Plus Machine.

The fabricated 3D structures were subsequently thermally treated in a SNOL 0.7/1250 tube furnace equipped with a quartz tube under a nitrogen atmosphere. The temperature was increased at a heating rate of 1°C/min to 600°C and maintained at this temperature for 3 h. After thermal treatment, the furnace was allowed to cool naturally to room temperature.

Characterisation

Optical images of the fabricated 3D structures were acquired using an OPTIKA Microscopes Italy optical microscope equipped with the PROview software. Surface images were recorded under both transmitted (bottom) and reflected (top) illumination conditions to visualise the morphology of the printed structures.

Fourier-transform infrared (FTIR) spectroscopy was performed using a Bruker Alpha spectrometer. Spectra were recorded in a wavenumber range of 4000–400 cm^{-1} with a spectral resolution of 2 cm^{-1}.

X-ray diffraction (XRD) analysis of the thermally treated samples was carried out using a Rigaku SmartLab SE diffractometer over a 2θ range of 10–80°, employing Cu Kα radiation and a Ni filter. Prior to analysis, the 3D structures were ground into fine powders using an agate mortar.

Thermogravimetric analysis (TGA) of the polymeric sample was conducted using a PerkinElmer Pyris 1 TGA instrument. The measurements were performed under a nitrogen atmosphere with a heating rate of 5°C/min up to 900°C.

The absorption spectra of the solutions were recorded using a PerkinElmer Lambda 35 UV/Vis spectrophotometer in a wavelength range of 350–700 nm with a measurement interval of 1 nm. Sarstedt polystyrene cuvettes with a 1 cm optical path length were used for all measurements.

Evaluation of photocatalytic properties

To evaluate the photocatalytic activity of the annealed 3D structures, the degradation of RhB dye in an aqueous solution was investigated. A halogen lamp (Radium RJL 5012 FL) was selected as the irradiation source due to its spectral distribution closely resembling that of solar radiation in the visible and infrared regions [13]. The lamp irradiation spectrum is available on the official manufacturer's website [14]. The lamp operated at 12 V with a nominal current of 4.17 A. Its rated luminous flux was 510 lm, with a luminous intensity of 2600 cd, a beam angle of 24°, an efficacy of 10.2 lm/W, and a colour temperature of 3000 K. The photocatalytic experiments were conducted simultaneously for the entire series of 3D photocatalyst structures, comprising three different structural densities, while maintaining identical experimental conditions, including the distance between the light source and the samples, stirring rate, volume of the RhB solution, and its initial concentration.

The photocatalytic activity measurements were performed according to the following procedure. First, 50 mL of an aqueous RhB solution (10 mg/L) was added to 150 mL glass beakers containing the annealed 3D structures. The dye solution was prepared by dissolving 10 mg of RhB in 1 L of deionised water. After confirming that the structures were fully immersed in the solution, magnetic stirring was initiated at 400 rpm. The beakers were then kept in the dark for 1 h to allow the adsorption–desorption equilibrium to be established through the physical adsorption of the dye onto the photocatalyst surface. Following this dark equilibration period, an aliquot was collected from each beaker and the absorbance of the solutions was measured using a PerkinElmer Lambda 35 UV–Vis spectrophotometer. Measurements were carried out using 1 cm path-length polystyrene cuvettes (Sarstedt), and the analysed solutions were subsequently returned to their respective beakers to maintain a constant reaction volume. The halogen lamp was then switched on to initiate photocatalysis. Absorption spectra of the RhB solutions were recorded every 15 min during the first hour of irradiation and subsequently every 30 min until a total irradiation time of 150 min was reached.

RESULTS AND DISCUSSION

Assessment of material chemical composition

Investigation of the chemical composition and structural transformations occurring during photopolymerisation and subsequent thermal treatment is essential for understanding the formation

of boron nitride-based photocatalysts and correlating their chemical structure with their photocatalytic performance in water treatment applications. To characterise the materials used and evaluate changes in their chemical composition throughout processing, Fourier-transform infrared (FTIR) spectroscopy was performed. The obtained spectra are presented in Fig. 2, where the characteristic absorption bands and peaks of the investigated materials are indicated.

The FTIR spectrum of the BN precursor (Fig. 2a) exhibits two characteristic absorption bands typical of hexagonal boron nitride: a band at 1335 cm^{-1} corresponding to B–N stretching vibrations and a band at 765 cm^{-1} assigned to B–N–B bending vibrations. No impurity-related or other significant absorption bands were observed in the BN spectrum, indicating the high purity of the starting material.

FTIR analysis was also carried out for the prepared photopolymer resin before and after the incorporation of BN particles (Fig. 2b, c). The spectra contain characteristic absorption bands associated with the resin components, HEMA and TMPEOTA. Bands common to both monomers were observed at approximately 2900 cm^{-1}, corresponding to aliphatic C–H stretching vibrations, and at 1715 cm^{-1}, attributed to the carbonyl (C=O) stretching vibrations of the ester groups present in both HEMA and TMPEOTA. A distinct absorption band at 1636 cm^{-1} was assigned to the stretching vibrations of carbon–carbon double bonds (C=C) characteristic of the monomeric species. The band at 1165 cm^{-1} corresponds to C–O–C stretching vibrations, further confirming the presence of ester functionalities. Additionally, a broad absorption band around 3500 cm^{-1}, characteristic of O–H stretching vibrations, was observed and can be attributed exclusively to the hydroxyl group present in the HEMA structure. It is noteworthy that the FTIR spectrum of the BN-containing resin (Fig. 2c) exhibited an overall increase in signal intensity within the 1500–1000 and 800–500 cm^{-1} regions. This enhancement originates from the characteristic vibrational modes of BN observed in the precursor spectrum (Fig. 2a), confirming the successful incorporation of BN particles into the resin matrix.

The FTIR spectrum of the fabricated 3D structures after photopolymerisation (Fig. 2d) revealed the disappearance of the absorption band at 1636 cm^{-1} that was present in the spectra of the uncured resins (Fig. 2b, c). The absence of this C=C related band indicates the consumption of the double bonds during photopolymerisation and confirms the successful polymerisation of both HEMA and TMPEOTA. Furthermore, the characteristic BN bands at 1335 and 765 cm^{-1} became clearly visible, while the intensity of the monomer-related absorption bands decreased substantially.

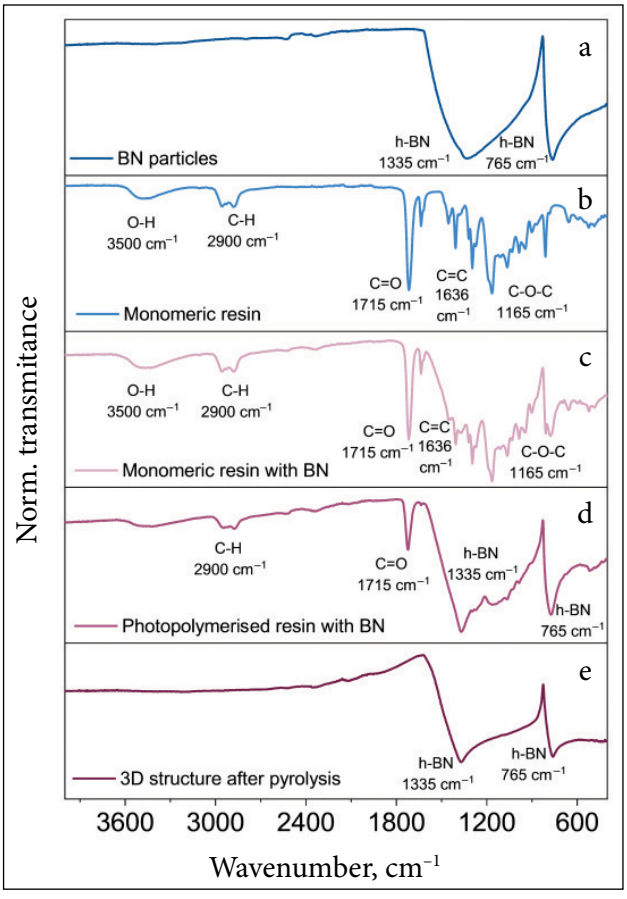

Fig. 2. FTIR spectra of the materials at different stages of preparation: (a) the BN particles reagent; (b) the prepared liquid resin containing the TPO photoinitiator; (c) the liquid resin containing both the TPO photoinitiator and BN particles; (d) the polymerised photopolymer resin; (e) the annealed 3D structure

Following thermal treatment, the FTIR spectrum of the annealed 3D structures (Fig. 2e) contained only the characteristic BN absorption bands observed in the precursor material (Fig. 2a). In addition, these BN-related bands became noticeably sharper after annealing. This effect may be attributed to the presence of amorphous carbon residues formed during the pyrolysis of the photopolymer resin. The complete absence of resin-related absorption bands in the annealed sample spectrum confirms that the organic resin underwent full thermal decomposition and that the resulting volatile

decomposition products were effectively removed during the annealing process.

Visual assessment of 3D structure quality

The quality, appearance, and structural defects of the fabricated 3D structures were evaluated through visual inspection and optical microscopy. A total of nine printed 3D structures were investigated, including three gyroid-based structures with different periodicities (3-period, 4-period and 7-period gyroid structures), three honeycomb-shaped lattices (2 × 3, 3 × 4 and 4 × 5 honeycomb lattices), and three cubic lattices (2 × 2, 3 × 3 and 4 × 4 cubic lattices) [15]. The photocatalytic efficiency of a 3D photocatalyst is strongly influenced by its accessible surface area, light penetration and distribution within the structure, and the mass transport of the liquid through the photocatalyst during operation [9, 16, 17]. Unlike conventional powder photocatalysts, architected 3D structures enable these parameters to be precisely tailored through a geometric design. Consequently, the optimisation of the 3D architecture represents a key strategy for enhancing photocatalytic performance. Representative photographs of the fabricated 3D structures are presented in Fig. 3.

Visual inspection of the structures presented in Fig. 3 revealed a clear trend of decreasing fabrication quality with increasing structural periodicity. In addition, the internal cavities of the 3D structures became progressively filled with the photopolymer resin during printing, and this residual resin could not be completely removed during the post-printing washing process. This effect was most pronounced in the 7-period gyroid structure shown in Fig. 3c. Among the investigated geometries, the honeycomb-shaped lattice series (Fig. 3d–f) exhibited the least adverse impact of increasing periodicity on structural quality. Comparison of the fabricated structures with their corresponding CAD models indicated that structures with lower periodicity (Fig. 3a, d, g) were reproduced with the highest fidelity.

Nevertheless, the 2 × 2 cubic lattice shown in Fig. 3g underwent deformation during the removal of the support structures generated for the printing process, which had partially fused with the printed architecture. The filling of structural cavities with residual resin is expected to reduce the photocatalytic efficiency of the fabricated catalysts by decreasing the accessible active surface area. To more precisely evaluate the quality of the fabricated structures,

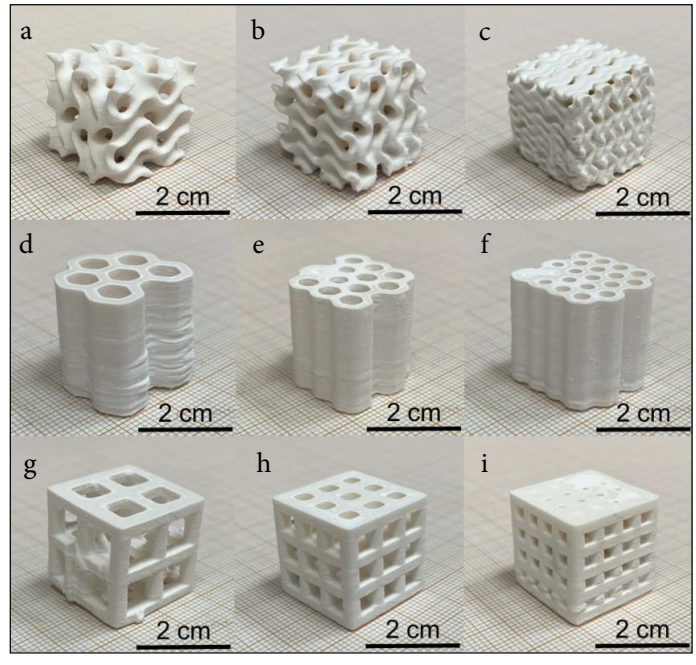

Fig. 3. Printed 3D structures: (a–c) gyroid-based 3D structures with different periodicities (3-period, 4-period and 7-period gyroid structure); (d–f) honeycomb-shaped 3D lattices (2 × 3, 3 × 4 and 4 × 5 honeycomb lattice); (g–i) cubic 3D lattices (2 × 2, 3 × 3 and 4 × 4 cubic lattice). Within each series, the structures are arranged according to their structural periodicity

the surfaces of the printed 3D architectures were examined using optical microscopy. The results of this analysis are presented in Fig. 4.

As can be seen from the images presented in Fig. 4, the 3D structures with the lowest structural periodicity (Fig. 4a, d, g) exhibited the highest quality. Their structural cavities were either completely open or only minimally obstructed, and no surface cracks were observed. The optical microscopy images confirmed the trend identified in the visual inspection (Fig. 3), namely that increasing structural periodicity leads to a reduction in printing quality, primarily due to the progressive filling of structural cavities with residual photopolymer resin. Furthermore, small surface cracks were observed in structures with intermediate periodicity (Fig. 4b, e, h) as well as in those with the highest periodicity (Fig. 4c, f, i). As the complexity and periodicity of the 3D architectures increase, the structural defects such as cracks and partially blocked cavities also increase. It is worth noting that the 4 × 5 honeycomb lattice, representing the highest-periodicity structure within the honeycomb series (Fig. 4f), exhibited the least cavity blockage by residual photopolymer resin when compared with the highest-periodicity structures of the gyroid and cubic series (Fig. 4c, i, respectively).

To remove the organic component of the photopolymer resin, the printed 3D structures were annealed at 600°C under a nitrogen atmosphere. The morphology and structural integrity of the annealed samples were subsequently evaluated through visual inspection and optical microscopy. Representative images of the annealed 3D structures are presented in Fig. 5. All printed 3D structures underwent significant shrinkage during thermal treatment and turned black in colour. The honeycomb- and cubic-shaped 3D lattices (Fig. 5d–i) exhibited noticeable changes in their overall geometry after annealing. The most severe structural deformations were observed in the cubic lattices (Fig. 5g–i), whose surfaces became concave and exhibited non-uniform shrinkage. This uneven shrinkage can be attributed to pre-existing structural defects, variations in wall thickness, and non-uniform heat distribution throughout the structures during heating. The observed surface depressions are likely attributable to non-uniform pyrolysis, in which thermal decomposition occurred earlier in the outer regions of the structures, while the interior regions decomposed at a later stage, resulting in differential shrinkage.

In addition, cubic lattices are more susceptible to the development of localised stress concentrations

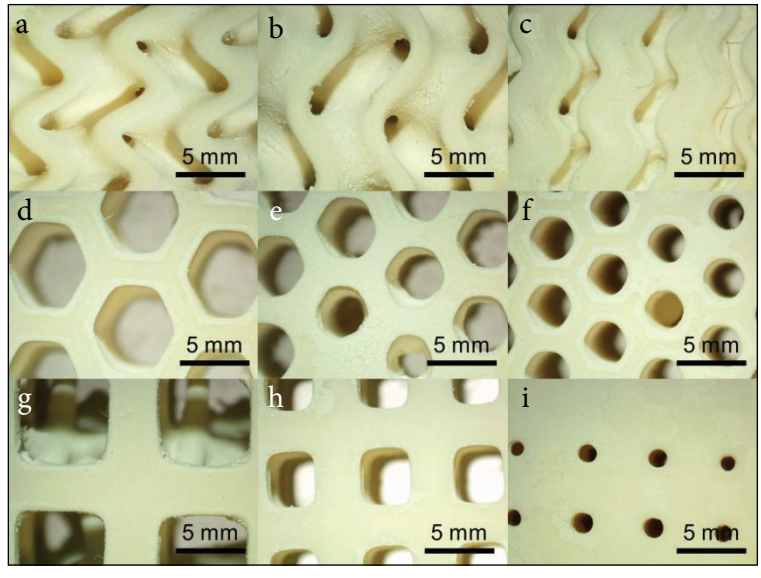

Fig. 4. Surface micrographs of the printed 3D structure series: (a–c) gyroid-based 3D structures with different periodicities (3-period, 4-period and 7-period gyroid structure); (d–f) honeycomb-shaped 3D lattices (2 × 3, 3 × 4 and 4 × 5 honeycomb lattice); (g–i) cubic 3D lattices (2 × 2, 3 × 3 and 4 × 4 cubic lattice). Within each series, the surface images are arranged according to the structural periodicity of the corresponding structures

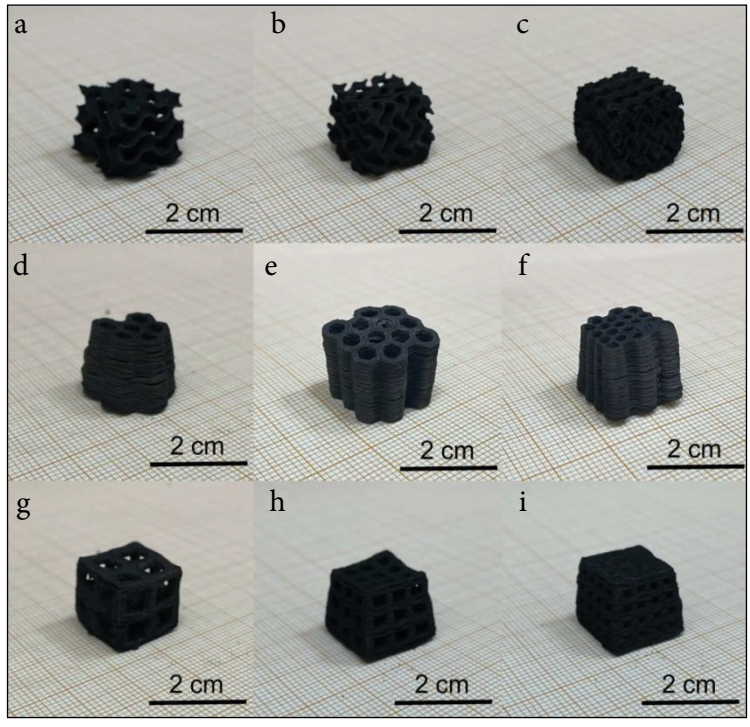

Fig. 5. Series of annealed 3D structures: (a–c) gyroid-based 3D structures with different periodicities (3-period, 4-period and 7-period gyroid structure); (d–f) honeycomb-shaped 3D lattices (2 × 3, 3 × 4 and 4 × 5 honeycomb lattice); (g–i) cubic 3D lattices (2 × 2, 3 × 3 and 4 × 4 cubic lattice). Within each series, the structures are arranged according to their structural periodicity

during pyrolysis, particularly at corners and other sharp structural features. These stress concentrations promote localised deformation, resulting in the more pronounced distortions observed in the cubic architectures. In contrast, the gyroid-based 3D structures (Fig. 5a–c) exhibited a minimal deformation following thermal treatment, demonstrating a superior structural stability. Similar to the observations made prior to annealing (Fig. 3), the cavities of structures with a higher structural periodicity remained partially filled with residual material, resulting in reduced pore accessibility.

The surfaces of the annealed 3D structures were further examined using optical microscopy. Representative surface micrographs of the annealed samples are presented in Fig. 6. Following thermal treatment, a clear trend emerged: the number of surface cracks increased with increasing structural periodicity. These cracks are attributed to the non-uniform densification and shrinkage of the structures during thermal treatment. As the organic resin underwent pyrolysis and decomposed, localised differences in shrinkage within the structures led to crack formation. Among the investigated geometries, the honeycomb-shaped 3D lattices (Fig. 6d–f) exhibited the lowest amount of surface cracks, indicating a greater ability to maintain structural integrity during annealing.

Thermal conversion of 3D structures

Thermogravimetric analysis (TGA) was performed on fragments of the printed 3D structures to evaluate the evaporation and thermal decomposition processes occurring during heating. The TGA results are presented in Fig. 7.

As shown by the TG and mass loss rate (DTG) curves in Fig. 7, the pyrolysis of the printed 3D structures proceeded in two distinct stages. During the first stage (up to 150°C), the removal of adsorbed moisture and volatile organic species, including residual unpolymerised resin, was observed. This stage was accompanied by a 2.8 wt.% mass loss, with a maximum mass loss rate of –0.51% min^{-1} at 110°C. No significant mass changes were detected between the first and second stages, indicating that the material remained thermally stable within this temperature range.

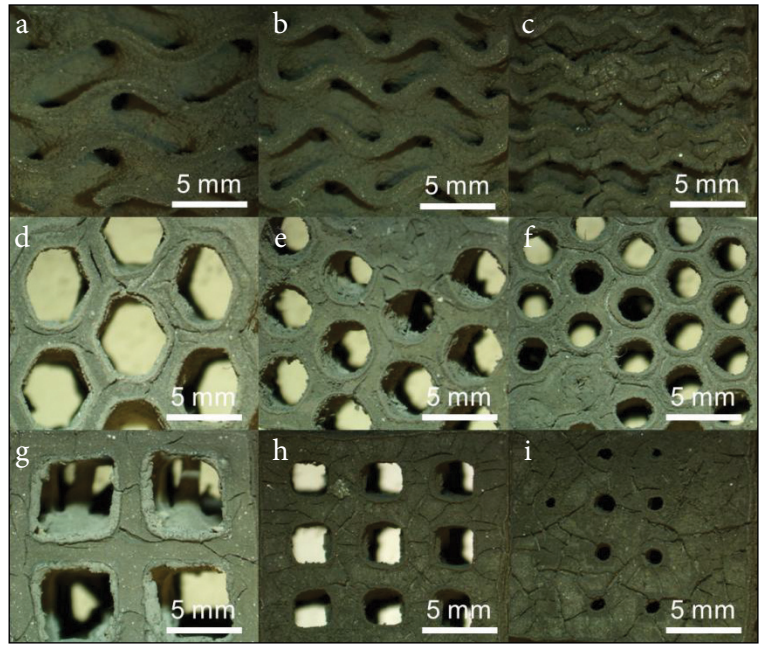

Fig. 6. Optical microscopy images of the surfaces of the annealed 3D structures: (a–c) gyroid-based 3D structures with different periodicities (3-period, 4-period and 7-period gyroid structure); (d–f) honeycomb-shaped 3D lattices (2 × 3, 3 × 4 and 4 × 5 honeycomb lattice); (g–i) cubic 3D lattices (2 × 2, 3 × 3 and 4 × 4 cubic lattice). Within each series, the surface micrographs are arranged according to the structural periodicity of the corresponding structures

The second stage, occurring between 325 and 450°C, corresponded to the thermal decomposition of the polymeric matrix. A substantial mass loss of 66.2 wt.% was recorded, with the maximum mass loss rate reaching –8.35% min^{-1} at 43°C. This pronounced weight loss indicates an intensive degradation of the organic components and the cleavage of the polymer network, consistent with previous reports [18]. Following the completion of this stage (>450°C), no further significant mass loss was observed, suggesting that the degradation of the organic fraction was essentially complete.

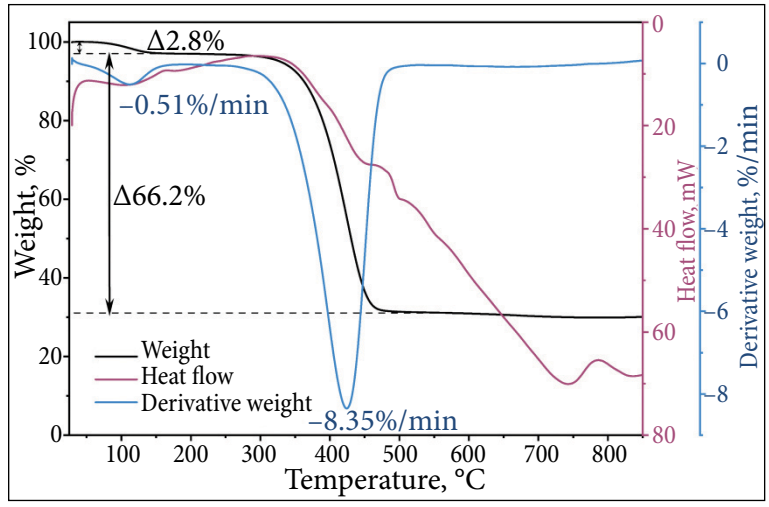

Fig. 7. Thermogravimetric analysis (TGA) of fragments of the printed 3D structures. The black curve represents the mass fraction (TG), the blue curve shows the mass loss rate (DTG), and the pink curve shows the heat flow (DSC)

The remaining residue is therefore attributed to thermally stable inorganic phases and amorphous carbon.

The heat flow (DSC) curve (Fig. 7, a pink curve) exhibited a weak endothermic effect during the first stage (up to 150°C), corresponding to the evaporation of adsorbed moisture and volatile compounds. A pronounced endothermic peak was observed during the second stage (325–450°C), coinciding with the maximum mass loss and confirming that the decomposition of the polymeric network is an endothermic process. At temperatures above 450°C, a weak exothermic effect was detected, which can be attributed to carbonisation reactions leading to the formation of a carbonaceous residue.

Phase composition and crystallinity

To determine whether the crystal phase of the incorporated boron nitride (BN) remained unchanged after thermal treatment and whether any new crystalline phases had formed, X-ray diffraction (XRD) analysis was performed. The obtained diffraction patterns were compared with the reference pattern for hexagonal boron nitride (h-BN) from the Crystallography Open Database (COD 96-101-0603) [19]. The results are presented in Fig. 8.

The characteristic diffraction peaks of h-BN (COD 96-101-0603) are indicated in both diffraction patterns shown in Fig. 8a, b. The diffraction peaks of both the BN powder (Fig. 8a) and the annealed 3D structures (Fig. 8b) are in good agreement with the reference pattern of hexagonal boron nitride. Furthermore, no additional diffraction peaks were detected in the XRD pattern of the annealed 3D structures, indicating that no new crystalline phases were formed during thermal treatment. These results confirm that the BN retained its hexagonal crystal structure throughout the annealing process.

Photocatalytic performance of the fabricated 3D photocatalysts

The photocatalytic performance of the fabricated 3D photocatalysts was evaluated by monitoring the degradation of RhB in an aqueous solution under halogen lamp irradiation. Photocatalytic activity was determined from the decrease in RhB absorbance measured by UV–Vis spectrophotometry. The normalised UV–Vis absorption spectra are presented in Appendix Fig. A1–A3.

The gyroid structures (Fig. A1) exhibited a gradual decrease in RhB adsorption with increasing structural periodicity, which can be attributed to reduced solution permeability and a smaller accessible active surface area caused by fabrication defects, particularly clogged internal pores. All samples exhibited a continuous decrease in RhB absorbance with increasing irradiation time, confirming an effective photocatalytic degradation. However, photocatalytic activity decreased with increasing gyroid periodicity, with the three-period gyroid achieving the highest degradation efficiency owing to its larger accessible surface area and lower amount of defects.

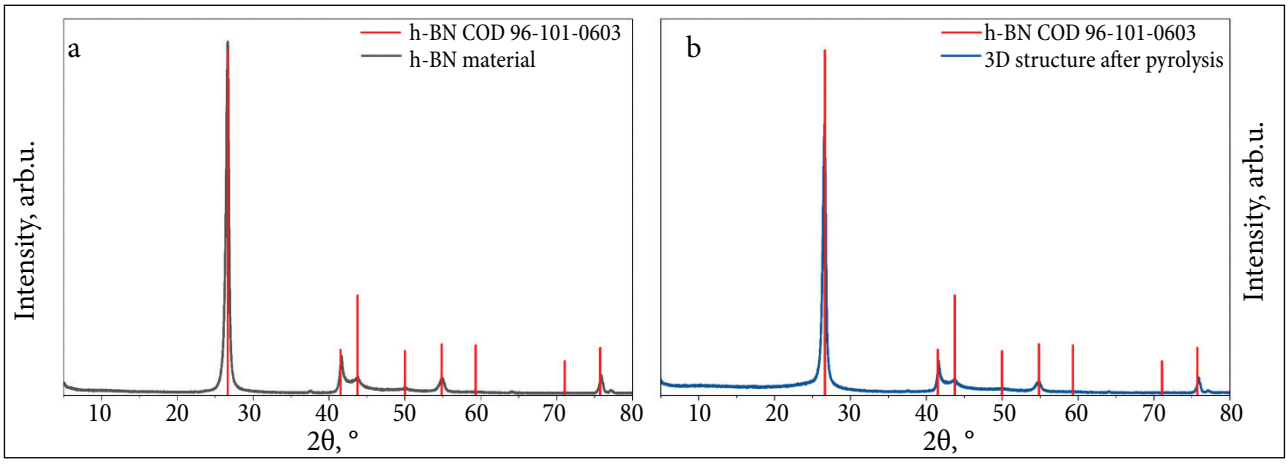

Fig. 8. X-ray diffraction (XRD) patterns. (a) XRD pattern of the h-BN reagent together with the corresponding reference pattern from the COD database (COD 96-101-0603). (b) XRD pattern of the annealed 3D structure together with the corresponding reference pattern from the COD database (COD 96-101-0603)

The photocatalytic performance of the honeycomb structures is shown in Fig. A2. Unlike the gyroid architectures, no clear correlation between adsorption capacity and structural periodicity was observed. The 3 × 4 honeycomb structure exhibited the best overall photocatalytic performance after 150 min of irradiation. Although denser honeycomb architectures generally demonstrated a higher activity, structural defects in the 4 × 5 honeycomb structure reduced its accessible active surface area and consequently its photocatalytic efficiency.

The cubic lattice structures (Fig. A3) exhibited a behaviour similar to that of the gyroid architectures. Physical adsorption decreased with increasing structural periodicity because of a restricted solution penetration and a reduced accessible surface area caused by clogged internal pores. All samples effectively degraded RhB under irradiation; however, photocatalytic activity declined with increasing periodicity. The 2 × 2 cubic lattice exhibited the highest degradation efficiency and, among all investigated architectures, produced the greatest decrease in RhB absorbance, demonstrating the best overall photocatalytic performance.

The photocatalytic performance of the printed 3D structures was quantitatively compared by evaluating the RhB degradation efficiency (%) as a function of irradiation time. The degradation efficiencies were calculated from the maximum integrated absorbance values of the UV–Vis spectra shown in Fig. A1–A3 insets. The resulting degradation profiles are presented in Fig. 9.

The degradation of RhB of the investigated 3D photocatalyst architectures are compared in Fig. 9, where each structure is represented by a different symbol. Throughout the photocatalytic experiment, the 2 × 2 cubic lattice exhibited the highest RhB degradation efficiency, whereas the seven-period gyroid showed the lowest performance. Similar photocatalytic behaviour was observed for the 3 × 4 honeycomb, three-period gyroid, and 3 × 3 cubic lattice structures, whose degradation curves remained close throughout the experiment and nearly overlapped after 150 min of irradiation. The investigated 3D architectures possessed different surface areas. Accurate determination of the surface area is essential for evaluating the photocatalytic performance of 3D structures, as the activity of a photocatalyst is directly related to the amount of accessible active surface available for photocatalytic reactions. Expressing photocatalytic efficiency per unit surface area enables a meaningful comparison of different architectures by isolating the effects of geometry on light propagation and mass transport while eliminating the influence of differences in total surface area [11, 20]. Therefore, the photocatalytic efficiency was normalised to the surface area of each structure and expressed as the amount of degraded RhB per unit surface area (mg/m^2).

The surface area of each architecture was calculated using the open-source software Blender from the measured dimensions (length, width and height) of the printed structures. It should be noted that these values represent theoretical surface areas, as structural defects introduced during thermal treatment were not considered in the calculations. The surface area-normalised photocatalytic efficiencies were determined from the degradation of

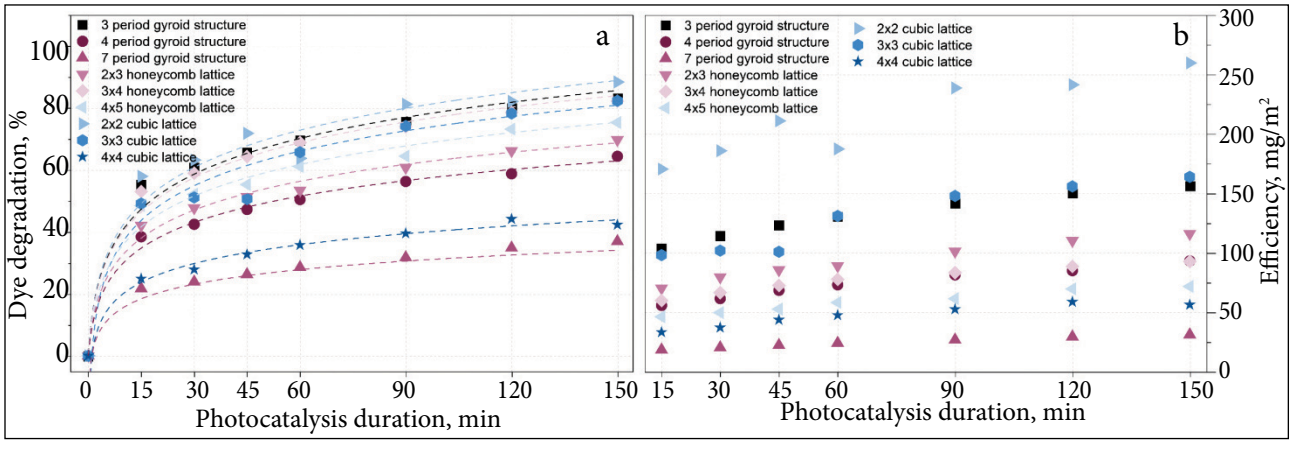

Fig. 9. RhB degradation efficiency (%) as a function of 3D structure architecture and photocatalytic irradiation time (a). Surface area-normalised RhB degradation efficiency (mg/m^2) as a function of 3D photocatalyst architecture and photocatalytic irradiation time (b)

RhB solutions with a known initial concentration, and the results are presented in Fig. 9b.

The surface area-normalised photocatalytic efficiencies of the investigated 3D architectures are compared in Fig. 9b, where each structure is represented by a different symbol. Throughout the photocatalytic experiment, the 2 × 2 cubic lattice exhibited the highest photocatalytic efficiency, reaching more than 255 mg/m^2 after 150 min of irradiation. This superior performance can be attributed to its open architecture, which allowed an efficient penetration of the dye solution and a uniform exposure of the entire structure to halogen lamp irradiation. In contrast, the seven-period gyroid exhibited the lowest photocatalytic efficiency, reaching only 30 mg/m^2 after 150 min. The poor performance of this architecture is attributed to its clogged internal pores, which restricted solution transport through the structure and substantially reduced the accessible photocatalytically active surface area.

Since practical photocatalysts should retain their activity during repeated use, the reusability of the printed 3D photocatalysts was investigated through consecutive RhB degradation experiments. The three-period gyroid structure was selected for this study because it exhibited a relatively high photocatalytic activity while possessing the fewest structural defects among the fabricated architectures. The normalised UV–Vis absorption spectra obtained during the reusability tests are presented in Appendix Fig. A4. The absorption spectra demonstrate that the decrease in RhB absorbance became progressively less pronounced with successive photocatalytic cycles, indicating a gradual decline in photocatalytic activity. A slight reduction in the physical adsorption capacity, represented by the red curve, was also observed after repeated use. Overall, the spectral data indicate that the photocatalytic performance gradually deteriorated with increasing the cycle number, with a particularly pronounced loss of activity observed during the third photocatalytic cycle (Fig. A4c).

To facilitate a quantitative comparison of the photocatalytic performance over repeated use, the RhB degradation efficiency (%) of the three-period gyroid photocatalyst was evaluated for three consecutive photocatalytic cycles. The degradation efficiencies were determined from the maximum integrated absorbance values of the normalised UV–Vis spectra shown in Fig. A4, and the results are presented in Fig. 10.

As shown in Fig. 10a, the photocatalytic degradation rate gradually decreased with the repeated use of the photocatalyst. After 150 min of irradiation, more than 70% of RhB was degraded during both the first and second photocatalytic cycles, whereas the degradation efficiency decreased to 47.5% during the third cycle. Compared with the first cycle, the second cycle exhibited a 9–13% lower degradation efficiency throughout the experiment, while the third cycle showed a further reduction of 22–36%. The observed non-linear decrease in photocatalytic activity suggests a gradual deterioration of the photocatalytically active surface during

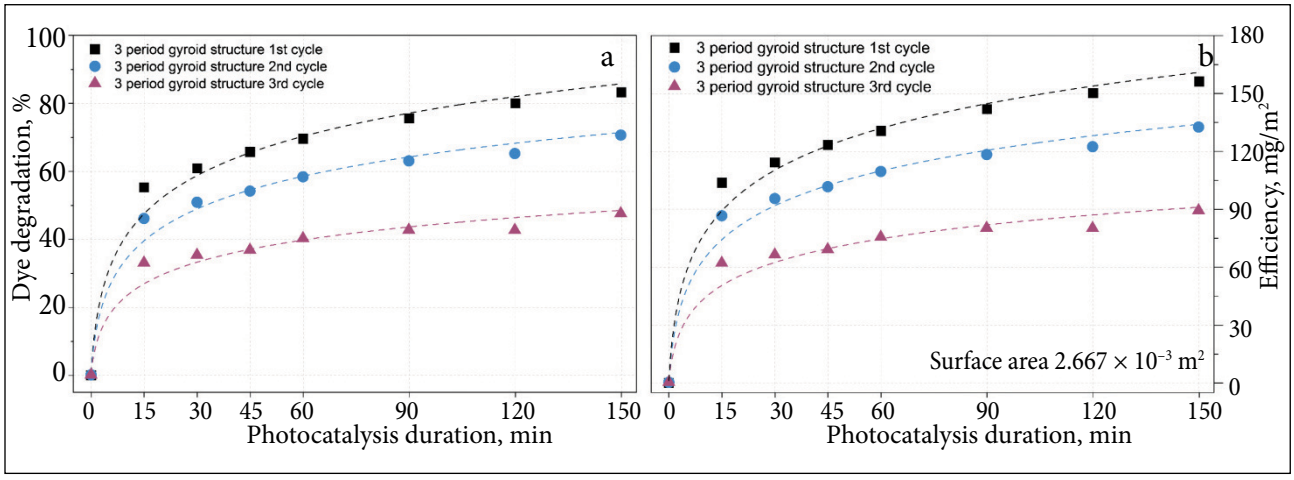

Fig. 10. RhB degradation efficiency (%) as a function of photocatalytic irradiation time for three consecutive cycles using the three-period gyroid photocatalyst (a). Surface area-normalised RhB degradation efficiency (mg/m^2) as a function of photocatalytic irradiation time over three consecutive cycles using the three-period gyroid photocatalyst (b)

the repeated use, leading to a reduction in the accessible active surface area.

To further evaluate the effect of repeated use on photocatalytic performance, the surface area-normalised degradation efficiency (mg/m^2) was determined for each photocatalytic cycle. The results are presented in Fig. 10b. A progressive decrease in the amount of degraded RhB per unit surface area was observed with increasing the cycle number. During the first two cycles, the photocatalyst maintained a high activity, achieving degradation efficiencies exceeding 130 mg/m^2 after 150 min of irradiation. However, efficiency decreased to 89 mg/m^2 during the third cycle. These results demonstrate that the repeated use leads to a gradual decline in photocatalytic performance. The reduced degradation efficiency indicates that regeneration of the photocatalyst may be required after prolonged operation.

Comparison of photocatalytic performance and structural characteristics

To facilitate a comprehensive comparison of the fabricated shape-controlled 3D photocatalyst architectures, the experimental results obtained in this study were systematically summarised in Table 1.

Analysis of the data summarised in Table 1 enabled the identification of the most efficient photocatalyst architecture within each structural series. Among the gyroid architectures, the three-period gyroid exhibited the highest photocatalytic performance, degrading 83.22% of RhB during a single 150 min photocatalytic cycle, corresponding to a surface area-normalised efficiency of 156.2 mg/m^2. This structure exhibited only minor structural deformation and a low density of defects, with its internal pores remaining largely unobstructed. Consequently, an efficient solution transport and a large accessible photocatalytically active surface area contributed to its superior performance within the gyroid series. In contrast, the seven-period gyroid demonstrated the lowest activity, degrading only 36.94% of RhB with a surface area-normalised efficiency of 30.9 mg/m^2. Its poor photocatalytic performance is attributed to severe pore clogging, which restricted the solution transport and substantially reduced the accessible active surface area.

Among the honeycomb architectures, the 3 × 4 honeycomb achieved the highest RhB degradation (82.27%). However, after the normalisation to the catalyst surface area, the 2 × 3 honeycomb exhibited the highest photocatalytic efficiency, reaching 116.1 mg/m^2. The decrease in efficiency observed for architectures with a higher periodicity is attributed to the increased number of fabrication defects, which reduced the accessible active surface area and consequently limited the photocatalytic performance.

Within the cubic lattice series, the 2 × 2 cubic lattice exhibited the highest photocatalytic activity, degrading 88.44% of RhB during a 150 min photocatalytic cycle and achieving the highest surface area-normalised efficiency of 259.9 mg/m^2. Although this architecture exhibited noticeable fabrication-related imperfections, including residual support marks and a non-uniform densification after the thermal treatment, its highly open architecture provided an excellent solution permeability and enabled an efficient illumination of the entire structure by the halogen lamp. Those characteristics maximised the accessible photocatalytically active surface area, resulting in the highest photocatalytic efficiency among all investigated architectures. Conversely, the 4 × 4 cubic lattice showed the lowest performance within that

Table 1. **Photocatalytic performance of the 3D photocatalysts after 150 min of degradation**

Photocatalyst architecture	Dye degradation, %	Efficiency, mg/m^2
3 period gyroid structure	83.22	156.2
4 period gyroid structure	64.42	93.2
7 period gyroid structure	36.94	30.9
2 × 3 honeycomb lattice	69.77	116.1
3× 4 honeycomb lattice	82.27	92.6
4 × 5 honeycomb lattice	75.36	71.6
2 × 2 cubic lattice	88.44	259.9
3 × 3 cubic lattice	82.33	164.0
4 × 4 cubic lattice	42.33	56.1

series, degrading only 42.33% of RhB and exhibiting a surface area-normalised efficiency of 56.1 mg/m^2. Similar to the gyroid structures, the reduced activity is attributed to clogged internal pores, which limited the solution accessibility and decreased the effective photocatalytically active surface area.

Overall, a clear trend was observed in which photocatalytic performance decreased with increasing structural periodicity. This behaviour is attributed to fabrication-induced defects, including clogged internal pores, residual support structures, and trapped photopolymer resin, which became increasingly difficult to avoid as the structural complexity increased. Those defects reduced both solution transport through the architectures and the accessible photocatalytically active surface area.

Among all investigated architectures, the 2 × 2 cubic lattice exhibited the highest photocatalytic performance (259.9 mg/m^2), followed by the 3 × 3 cubic lattice (164.0 mg/m^2). These findings demonstrate that an effective photocatalyst architecture should possess open, unobstructed internal channels that facilitate solution transport while allowing irradiation to penetrate deeply into the structure and uniformly illuminate the internal photocatalytically active surfaces.

To further assess the performance of the most efficient architecture, the photocatalytic activity of the 2 × 2 cubic lattice was compared with that of representative photocatalysts reported in the literature. The comparison is presented in Table 2.

Comparison of the fabricated h-BN 3D photocatalyst with the previously reported 3D photocatalytic architectures indicates that its RhB degradation efficiency is competitive, although not the highest among the systems considered. A ZnO photocatalyst with a similar 3D architecture achieved 97.73% degradation of a 10 mg/L RhB solution; however, a longer irradiation time (180 min) was required to reach this value [23]. In contrast, a TiO_2 photocatalyst with a 3D star-shaped architecture degraded 80% of RhB after a substantially longer photocatalytic treatment (240 min) [21]. A powdered TiO_2/g-C_3N_4 photocatalyst also demonstrated a higher degradation efficiency than the fabricated h-BN architecture under the same irradiation time (150 min) [22]. The h-BN-based photocatalysts reported in references [5] and [24] achieved higher photocatalytic efficiencies (99.94 and 93.70% after 120 min, respectively). However, the synthesis of their precursor materials is considerably more complex than the preparation of the photoresin used in the present work, highlighting the simplicity of the proposed fabrication approach. Despite its somewhat lower degradation efficiency compared with several previously reported systems, the fabricated h-BN 3D photocatalyst offers an important practical advantage over powder-based photocatalysts. Owing to its self-supporting architecture, it can be readily removed from the treated solution without requiring additional separation steps, thereby avoiding the recovery challenges commonly associated with suspended photocatalytic nanoparticles. Furthermore, although several reported 3D photocatalysts achieved higher RhB degradation efficiencies, the results suggest that extending the irradiation time could further improve the performance of the fabricated h-BN architecture. Reusability experiments demonstrated that the photocatalyst remained active over three consecutive photocatalytic cycles (450 min of cumulative irradiation), indicating a good operational stability and the potential for prolonged photocatalytic applications.

CONCLUSIONS

The present study demonstrated the feasibility of fabricating self-supporting h-BN-based 3D photocatalysts with controlled architectures by

Table 2. **Comparison of the fabricated 3D photocatalyst with previously reported photocatalysts**

Ref.	Photocatalyst	Architecture	Rhodamine B degradation, %	Irradiation time, min
This work	h-BN	3D 2 × 2 cubic lattice	88.44	150
[5]	BN	3D cage	99.94	120
[21]	TiO_2	3D star-shaped structure	80.00	240
[22]	TiO_2/g-C_{3N}4	Powder	96.00	150
[23]	ZnO	3D cubic lattice	97.73	180
[24]	h-BN	3D mesh-like walls gyroid	93.70	120

stereolithographic printing of a newly developed composite photoresin, followed by thermal treatment. The thermal treatment completely removed the polymer matrix while preserving the hexagonal BN crystal structure. In addition, the formation of amorphous carbon during pyrolysis is believed to reduce the band gap of h-BN, thereby enhancing its photocatalytic activity under visible-light irradiation. Reusability experiments demonstrated that the fabricated 3D h-BN photocatalysts retained a high photocatalytic activity during the first two degradation cycles, although a gradual decline in the degradation efficiency was observed upon the prolonged use. The photocatalytic evaluation further revealed that catalyst performance is governed not only by the available surface area but also by architectural features that influence the solution permeability, light penetration, and the accessibility of photocatalytically active sites. Among the investigated architectures, the 2 × 2 cubic lattice exhibited the highest surface area-normalised photocatalytic efficiency (259.9 mg/m^2), demonstrating that open architectures with large, unobstructed internal channels provide the most favourable combination of mass transport, light penetration, and accessible active surface. These findings provide practical design guidelines for the development of efficient, reusable, self-supporting h-BN photocatalysts for water treatment applications.

Received 15 July 2026
Accepted 22 July 2026

References

1. G. M. Shayo, E. Elimbinzi, G. N. Shao, C. Fabian, *Bull. Natl. Res. Cent.,* **47(1)**, 113 (2023) [https://doi.org/10.1186/S42269-023-01088-9].
2. L. Lin, H. Yang, X. Xu, *Front. Environ. Sci.,* **10** (2022) [https://doi.org/10.3389/fenvs.2022.880246].
3. N. Morin-Crini, E. Lichtfouse, G. Liu, et al., *Environ. Chem. Lett.,* **20(4)**, 2311 (2022) [https://doi.org/10.1007/S10311-022-01447-4].
4. T. Bekele, G. Alamnie, *Results Chem.,* **18**, 102758 (2025) [https://doi.org/10.1016/j.rechem.2025.102758].
5. R. Virkėtis, V. Klimkevičius, T. Murauskas, S. Šakirzanovas, L. Vilčiauskas, G. Merkininkaitė, *Adv. Eng. Mater.,* **28**, e202503003 (2026) [https://doi.org/10.1002/adem.202503003].
6. Y. Wang, Y. Zhang, S. Wang, Y. Guan, Y. Zhang, *Mater. Today Chem.,* **22**, 100566 (2021) [https://doi.org/10.1016/j.mtchem.2021.100566].
7. A. O. Yusuf, S. Al Jitan, R. Al Sakkaf, et al., *Appl. Mater. Today,* **35**, 101940 (2023) [https://doi.org/10.1016/j.apmt.2023.101940].
8. C. Xu, T. Liu, W. Wei, et al., *Adv. Eng. Mater.,* **22(3)**, 1901088 (2020) [https://doi.org/10.1002/adem.201901088].
9. S.-W. Bai, H. Mei, M.-G. Zhang, et al., *Mater. Today Nano,* **24**, 100385 (2023) [https://doi.org/10.1016/j.mtnano.2023.100385].
10. I. S. O. Barbosa, Y. A. Manrique, D. Paiva, J. L. Faria, R. J. Santos, C. G. Silva, *RSC Adv.,* **15(4)**, 2275 (2025) [https://doi.org/10.1039/D4RA07121B].
11. D.-S. Cheon, M. Takahashi, T. Kim, *J. Rock Mech. Geotech. Eng.,* **13(2)**, 368 (2021) [https://doi.org/10.1016/j.jrmge.2020.04.008].
12. L. Pan, M. Zhang, H. Mei, et al., *Sep. Purif. Technol.,* **301**, 121974 (2022) [https://doi.org/10.1016/j.seppur.2022.121974].
13. R. Peamsuwan, P. Waramit, I. Worapun, B. Krittacom, T. Phoo-Ngernkham, R. Luampon, *Energy Built Environ.,* **5(4)**, 517 (2024) [https://doi.org/10.1016/j.enbenv.2023.04.002].
14. Radium Lampenwerk GmbH, *Radium Lampenwerk GmbH* (2026) [https://www.radium.de/en].
15. N. Li, K. Tong, L. Yang, X. Du, *Mater. Today Energy,* **29**, 101100 (2022) [https://doi.org/10.1016/j.mtener.2022.101100].
16. B. Kaur, P. Singh, S. Thakur, et al., *J. Environ. Chem. Eng.,* **13(2)**, 116042 (2025) [https://doi.org/10.1016/j.jece.2025.116042].
17. Y. Majooni, S. P. Sava, K. Fayazbakhsh, N. Yousefi, *Adv. Sustain. Syst.,* **9(8)**, e00135 (2025) [https://doi.org/10.1002/adsu.202500135].
18. K. Demirelli, M. Coşkun, E. Kaya, *Polymer Degrad. Stabil.,* **72(1)**, 75 (2001) [https://doi.org/10.1016/S0141-3910(00)00204-4].
19. A. Brager, *Acta Physicochim.*, 699 (1937).
20. A. Chakraborty, O. Samriti, Ruzimuradov, R. K. Gupta, J. Cho, J. Prakash, *Environ. Res.,* **212**, 113550 (2022) [https://doi.org/10.1016/j.envres.2022.113550].
21. I. S. O. Barbosa, Y. A. Manrique, D. Paiva, J. L. Faria, R. J. Santos, C. G. Silva, *RSC Adv.,* **15(4)**, 2275 (2025) [https://doi.org/10.1039/D4RA07121B].
22. N. Madima, K. K. Kefeni, S. B. Mishra, A. K. Mishra, *Heliyon,* **8(9)**, e10683 (2022) [https://doi.org/10.1016/j.heliyon.2022.e10683].
23. G. Verma, M. Islam, A. Gupta, *Adv. Compos. Hybrid Mater.,* **8(1)**, 109 (2025) [https://doi.org/10.1007/S42114-024-01125-9].
24. G. Merkininkaitė, R. Virkėti, S. Šakirzanovas, *Next Mater.,* **12**, 102419 (2026) [https://doi.org/10.1016/j.nxmate.2026.102419].

APPENDIX

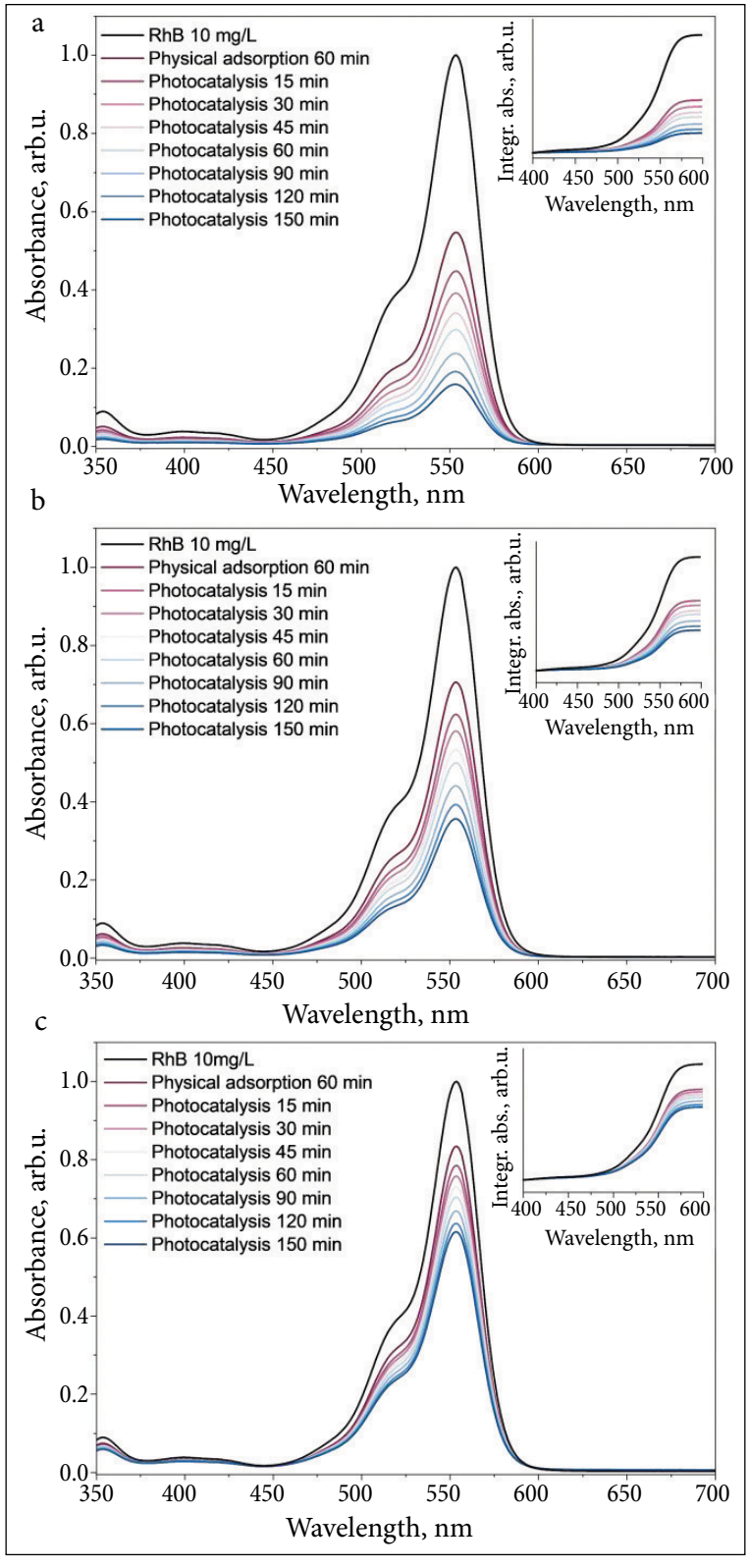

Fig. A1. UV–Vis absorption spectra of aqueous RhB solutions recorded before irradiation, after dark adsorption equilibrium, and after 15, 30, 45, 60, 90, 120 and 150 min of photocatalytic treatment under halogen lamp irradiation using gyroid photocatalysts: (a) three-period gyroid, (b) four-period gyroid and (c) seven-period gyroid

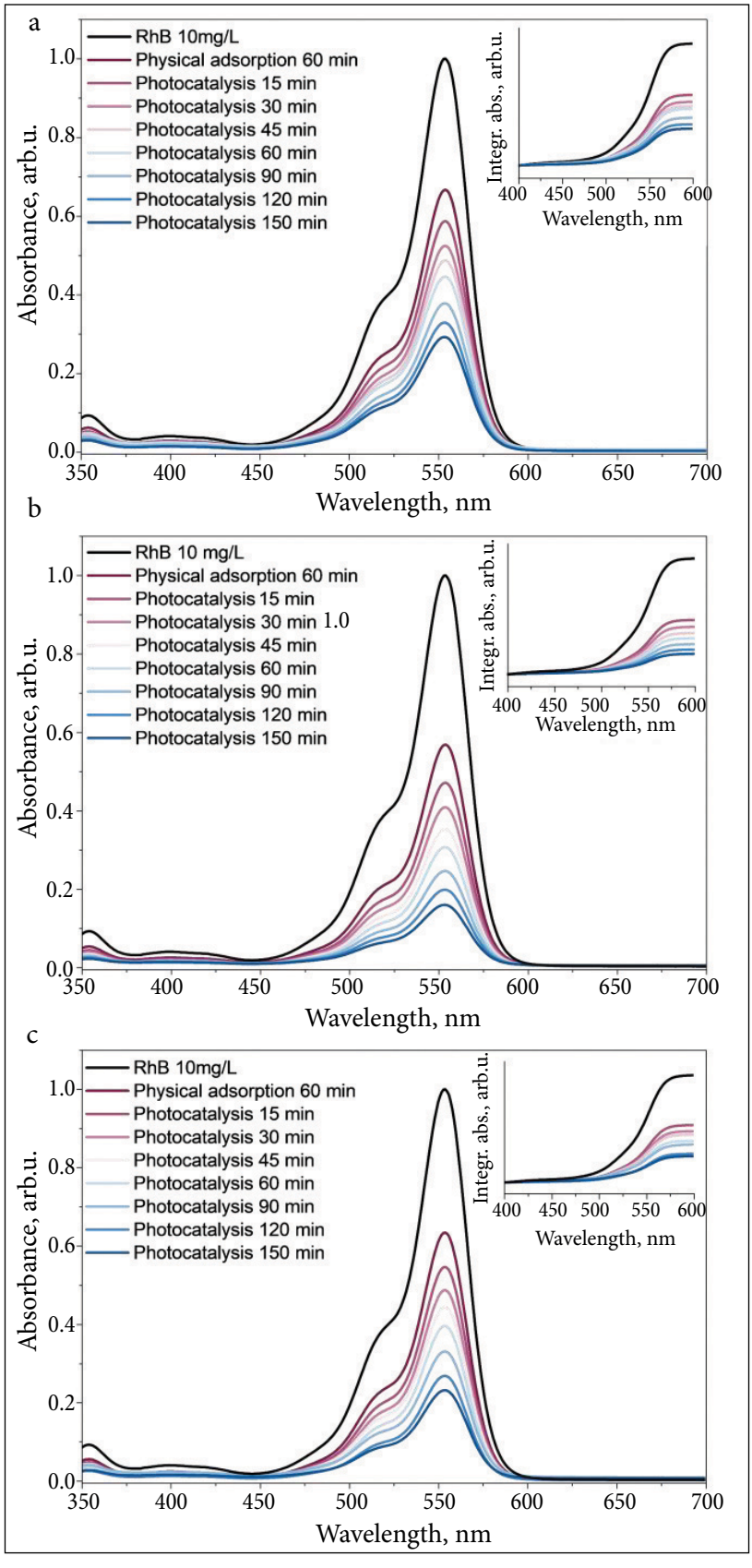

Fig. A2. UV–Vis absorption spectra of aqueous RhB solutions recorded before irradiation, after dark adsorption equilibrium, and after 15, 30, 45, 60, 90, 120 and 150 min of photocatalytic treatment under halogen lamp irradiation using honeycomb photocatalysts: (a) 2 × 3 honeycomb, (b) 3 × 4 honeycomb and (c) 4 × 5 honeycomb

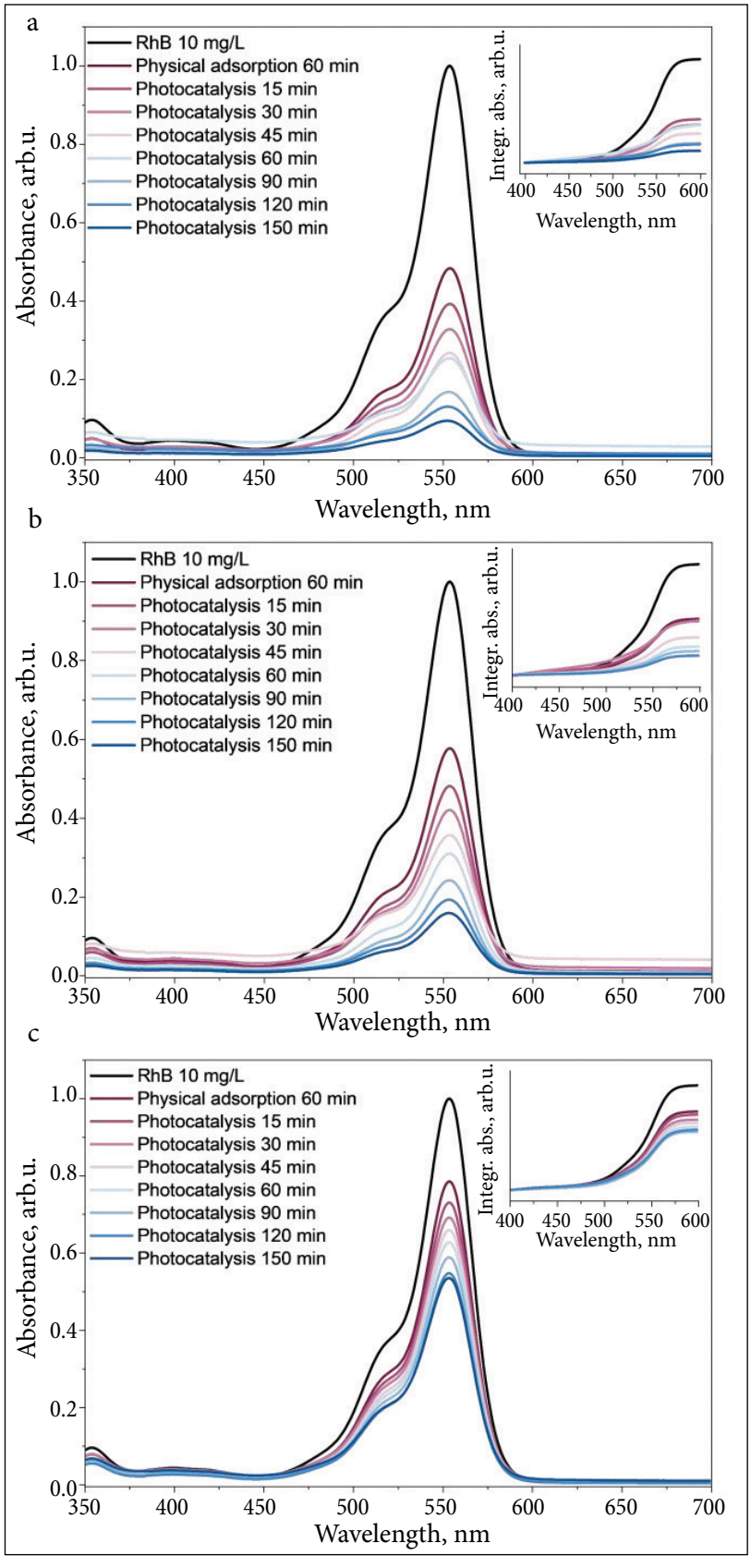

Fig. A3. UV–Vis absorption spectra of aqueous RhB solutions recorded before irradiation, after dark adsorption equilibrium, and after 15, 30, 45, 60, 90, 120 and 150 min of photocatalytic treatment under halogen lamp irradiation using cubic lattice photocatalysts: (a) 2 × 2 cubic lattice, (b) 3 × 3 cubic lattice and (c) 4 × 4 cubic lattice

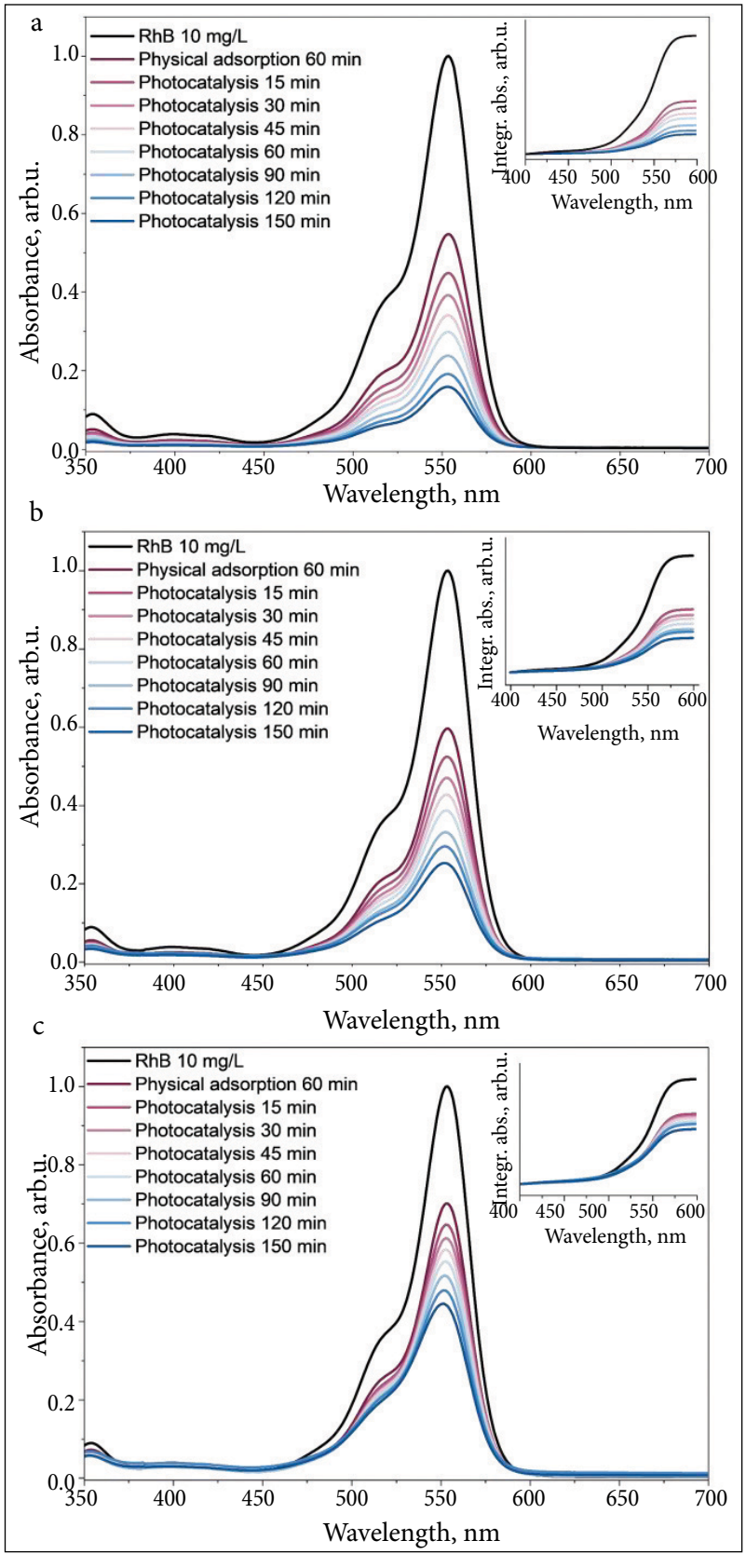

Fig. A4. UV–Vis absorption spectra of aqueous RhB solutions recorded before irradiation, after dark adsorption equilibrium, and after 15, 30, 45, 60, 90, 120 and 150 min of photocatalytic treatment under halogen lamp irradiation using the three-period gyroid photocatalyst: (a) the first photocatalytic cycle, (b) the second photocatalytic cycle and (c) the third photocatalytic cycle

Petras Rauka, Robertas Virkėtis, Simas Šakirzanovas, Greta Merkininkaitė

STEREOLITOGRAFIJOS BŪDU GAUTI BORO NITRIDO PAGRINDU SUKURTI 3D FOTOKATALIZATORIAI SU KONTROLIUOJAMA ARCHITEKTŪRA VANDENS VALYMUI

S a n t r a u k a

Naujai sukurta boro nitrido (BN) turinti kompozitinė fotoderva buvo panaudota kontroliuojamos geometrijos BN pagrindo fotokatalizatoriams gaminti, derinant stereolitografijos (SLA) ir pirolizės metodus. Suformuotos trijų tipų struktūros – giroidinės, korio ir kubinio narvelio – su skirtingu struktūriniu periodiškumu bei ištirta jų sandara ir fotokatalitinės savybės. 3D architektūros įtaka fotokatalitiniam efektyvumui įvertinta analizuojant Rodamino B (RhB) skilimą vandeniniame tirpale, apšviečiant halogeno lempa. Nustatyta, kad didėjant struktūriniam periodiškumui didėja gamybos defektų skaičius, mažėja tirpalo pralaidumas ir aktyvusis paviršiaus plotas, todėl blogėja fotokatalitinis efektyvumas. 2 × 2 kubinio narvelio struktūra, šviečiant halogeno lempai, per 150 min. suskaidė 88,44 % RhB ir pasiekė didžiausią pagal paviršiaus plotą normalizuotą fotokatalitinį efektyvumą – 259,9 mg/m^2. Gauti rezultatai rodo, kad taikant adityviosios gamybos technologiją galima sukurti efektyvius, daugkartinio naudojimo h-BN pagrindo 3D fotokatalizatorius.